COMPUTATIONALLY GUIDED IN-VITRO VASCULAR GROWTH MODEL REVEALS CAUSAL LINK BETWEEN FLOW OSCILLATIONS AND DISORGANIZED NEOTISSUE

E.E. VAN HAAFTEN[1,2], S. QUICKEN[3], W. HUBERTS[3], C.V.C. BOUTEN[1,2] ✉, AND N.A. KURNIAWAN[1,2]

ABSTRACT. Disturbed shear stress is thought to be the driving factor of neointimal hyperplasia in blood vessels and grafts, for example in hemodialysis conduits. Despite the common occurrence of neointimal hyperplasia, however, the mechanistic role of shear stress is unclear. This is especially problematic in the context of *in situ* scaffold-guided vascular regeneration, a process strongly driven by the scaffold mechanical environment. To address this issue, we herein introduce an integrated numerical-experimental approach to reconstruct the graft-host response and interrogate the mechanoregulation in dialysis grafts. Starting from patient data, we numerically analyze the biomechanics at the vein-graft anastomosis of a hemodialysis conduit. Using this biomechanical data, we show in an *in vitro* vascular growth model that oscillatory shear stress, in the presence of cyclic strain, favors neotissue development by reducing the secretion of remodeling markers by vascular cells and promoting the formation of a dense and disorganized collagen network. These findings identify scaffold-based shielding of cells from oscillatory shear stress as a potential handle to inhibit neointimal hyperplasia in grafts.

✉ C.V.C.Bouten@tue.nl

[1] Department of Biomedical Engineering, Eindhoven University of Technology, Eindhoven, The Netherlands

[2] Institute for Complex Molecular Systems (ICMS), Eindhoven University of Technology, Eindhoven, The Netherlands

[3] Department of Biomedical Engineering, CARIM School for Cardiovascular Diseases, Maastricht University, Maastricht, The Netherlands

Date: July 21, 2020.

INTRODUCTION (749 WORDS)

A major clinical problem in hemodialysis therapy for end-stage renal-diseased patients is vascular access dysfunction. Vascular access for long-term hemodialysis is achieved through native arteriovenous fistula (AVF) or synthetic arteriovenous graft (AVG). The primary cause of vascular access dysfunction in matured AVFs and AVGs is venous stenosis as a result of neointimal hyperplasia (NIH) [2]. The pathogenesis of venous NIH in vascular access is well described and thought to be initiated by, among other factors, fluid wall shear stress [3].

High shear stresses are persistently present in AVGs and AVFs, even years after vessel creation. Several studies have reported that regions with high wall shear stresses (in the range of 5–10 Pa) correspond to NIH formation [4, 5, 6]. On the other hand, Krishnamoorthy *et al.* has suggested an inverse correlation between wall shear stress (in the range of 5–80 Pa during peak flow) and stenosis formation [7]. It has also been proposed that low and oscillatory shear stress (in the range of <0.1–1 Pa) favors sites of stenosis [8] and that the temporal gradient of shear stress (in the range of $+0.5$ Pa/week up to 3.5 Pa) correlates with intimal medial thickening [9, 10]. These seemingly inconsistent findings raise important questions about both the mechanistic foundation and the validity of the conjecture that wall shear stress stimulates the initiation and development of NIH in vascular access vessels. Indeed, systematic reviews reveal that the clinical evidence for this disturbed flow theory is weaker than generally believed and that so far very little is known about how altered flow is related to the cellular processes underlying NIH [11, 12].

The need for mechanistic insights in (patho)physiological situations is especially critical with the emergence of a relatively new paradigm in regenerative medicine: *in situ* tissue engineering (TE). This strategy hinges on the implantation of directly functional, bioresorbable, cell-free scaffolds, e.g., to be used as vascular access grafts (AVGs), which direct tissue regeneration at the locus of implantation to grow the neotissue into a state of mechanical homeostasis, presumably reducing the risk of NIH. The merit of the TE approach was recently highlighted in a study by Kirkton *et al.*, where the authors implanted a bioengineered, acellular, human vessel as a hemodialysis conduit in patients with end-stage renal disease [13]. These vessels completely recellularized in this complex *in vivo* environment and transformed into a functional, living tissue, allowing repeated cannulation for years.

The new tissue has, so to say, 'emerged' from its complex *in vivo* environment, whose convolution of individual factors, such as the interaction between cells and their 3D environment, paracrine and juxtracrine signals from other cells, and response to mechanical forces, determined the resulting tissue properties. Intriguingly, these factors also affect the secretion of proteinases (e.g., MMPs and TIMPs), cytokines (e.g., MCP-1 and IL-6), and growth factors (e.g., TGF-β1), which are known to be involved in NIH formation [11]. To advance this promising therapeutic development, it is of paramount importance to dissect this complexity, because the knowledge about the role of each factor and the interplay between these factors provides crucial design parameters for guiding the developing tissue towards mechanical homeostasis [14].

In the present study, we introduce a numerical-experimental approach to systematically investigate how neotissue develops under the influence of the demanding hemodynamic environment in regenerating AVG-scaffolds (Scheme 1). To quantitatively parameterize this environment, we use computational fluid dynamics (CFD) and fluid structure interaction (FSI) modeling of a clinically-derived vein-graft anastomosis. We then simulate this environment using our recently developed *in vitro* model system [15]. This *in vitro* system is used to mimic the (early) pro-inflammatory stages of scaffold-driven *in situ* tissue formation, based on (1) the co-culture of human tissue-producing vascular cells and macrophages, which are (2) seeded in electrospun grafts, and (3)
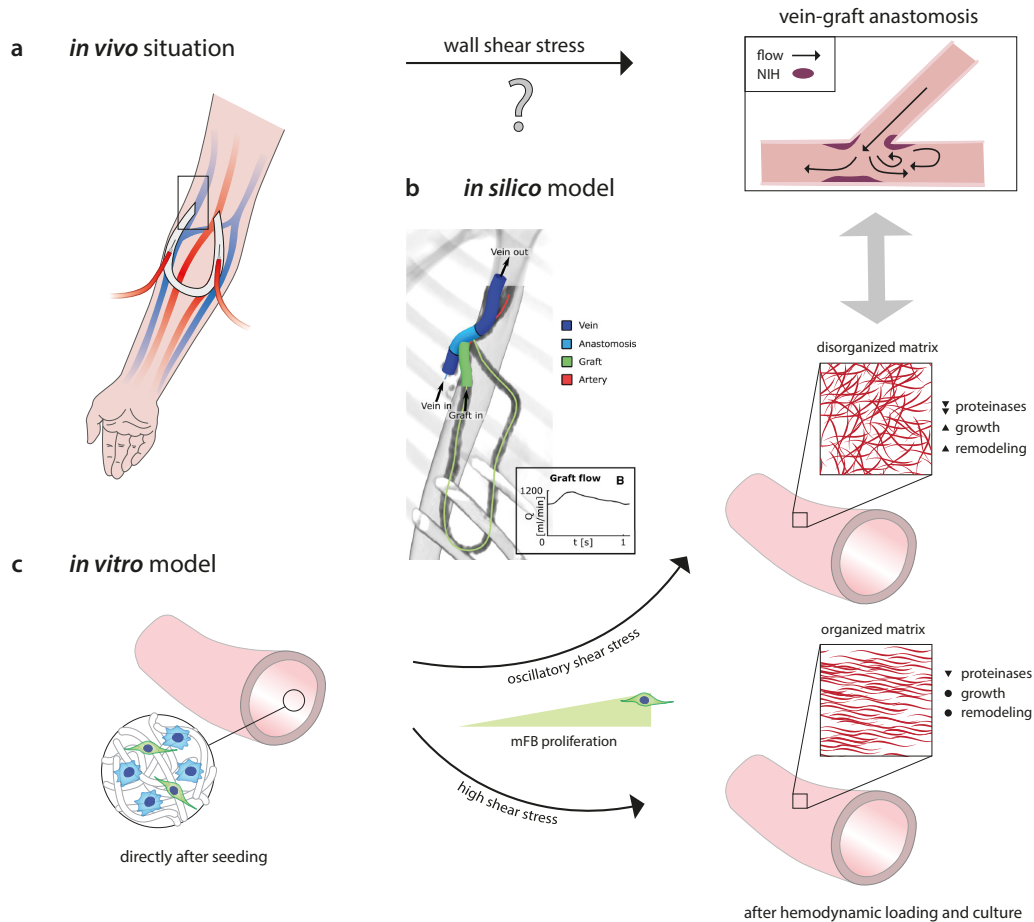
SCHEME 1. **Proposed role of shear stress on *in vivo* neointimal hyperplasia, as revealed from a combined *in silico* and *in vitro* study. (a)** *In vivo*, neointimal hyperplasia at the venous anastomosis of vascular access grafts is a common occurrence. This pathology is presumably driven by shear stress. **(b)** Using *in silico* models (i.e., computational fluid dynamic (CFD) and fluid structure interaction (FSI) models), the mechanical environment (i.e., the shear stresses and strains) in vascular access grafts is computed. **(c)** The results of these *in silico* models are used to define the boundary conditions for the *in vitro* model (i.e., a 3D scaffold containing macrophages and (myo)fibroblasts (mFBs)), in which the computed shear stresses and strains are recapitulated. After 14 days of dynamic culture, allowing for mFB proliferation and tissue formation, oscillatory shear stress resulted in a reduction of several proteinases and upregulation of growth and remodeling markers, which was accompanied by a dense and disorganized appositional matrix structure. This in contrast to high shear stress, which led to a strongly aligned appositional matrix. Note that in the *in vitro* study the shear stress and matrix alignment did not occur at the luminal side but at the outside of the scaffold. Panel b is reproduced with permission [1].

58 cultured in a bioreactor platform that allows for the independent control of wall shear stress and
59 strain. This unique approach allows the delineation of the roles of biomechanical tissue environment
60 and cellular responses, as well as their interplay, in scaffold-guided vascular tissue formation.

61 The findings revealed that various wall shear stress metrics (low, high, and oscillatory), in the
62 presence of cyclic strain, differently regulate NIH- and tissue growth-related protein secretion,
63 tissue growth, and remodeling. In particular, oscillatory shear stress promoted the formation of
64 a dense and disorganized collagen network. Together, these insights confirm for the first time the
65 causative relationship between different shear stress modes and biological responses, and contribute
66 to an improved understanding of scaffold-guided tissue regeneration and the initiation mechanism
67 of neointimal hyperplasia in vascular access vessels.

68   RESULTS & DISCUSSION (2397 WORDS)

69 **Hemodynamics at the NIH-prone sites in the AVG.** In the early stages of *in situ* scaffold-
70 guided vascular regeneration, the scaffold largely determines the mechanical performance of the
71 overall construct. To quantitatively understand the hemodynamic environment in the NIH-prone
72 sites of these scaffolds when implanted as AVG, we computed the local hemodynamics using numer-
73 ical models (Fig. 1a). For this purpose, a realistic AVG geometry was reconstructed from 15 months
74 post-operative CTA (computed tomography angiography) scans and two weeks-preoperative ultra-
75 sound diameter measurements of a single renal-diseased patient. For detailed information regarding
76 the model reconstruction and numerical simulations, the reader is referred to the Methods.

77 The flow disturbances at the perianastomotic region at the venous site are known to cause the
78 most common graft-related complications. These flow disturbances are associated with the local
79 deformations and local shear stresses of the venous perianastomotic wall. To accurately estimate
80 these local stresses and strains, we developed an FSI model of this region, which took into account
81 the temporally-varying flow-induced wall deformations as well as the consequent flow profiles. The
82 graft (0.63 mm wall thickness) and the vein (0.385 mm wall thickness) were modeled as a Neo-
83 Hookean material, with a Young's modulus of 1.5 MPa for the graft [16] and 0.455 MPa for the
84 vein [1]. A CFD model of the full geometry with a rigid wall assumption was used to obtain proper
85 boundary conditions for the FSI model and to estimate the wall shear stresses in the graft. At
86 the inlet boundary of the CFD model, a Doppler ultrasound-based velocity profile was prescribed,
87 whereas at the proximal venous outlet a zero-pressure boundary condition was prescribed [17]. To
88 mimic the peripheral bed and collateral venous flow, a six-elements lumped parameter model was
89 coupled to the distal arterial and venous outlets.

90 These simulations revealed that the shear stresses have time-averaged values of around 5 Pa with
91 a low oscillatory shear index (OSI, Fig. 1c). The shear stresses are in the same order of magnitude
92 compared to previous studies that focus on shear stress in vascular access vessels (mostly AVFs
93 [18, 19]). The strains around the venous anastomotic border are in the order of 1 % with extremes
94 up to 2 % at the anastomosis (Fig. 1b). To the best of our knowledge, this is the first study that
95 quantifies strains in AVGs, giving a unique insight into the biomechanical environment inside these
96 AVGs.

97 **Integrating computational output into *in vitro* model.** The biomechanical environment in
98 the AVGs, as quantified from these computational outputs, were mimicked in our *in vitro* platform
99 to recapitulate the local hemodynamics in vascular access vessels, i.e., the shear stresses and strains,
100 allowing us to directly correlate to a biological response. This approach provides possibilities to test
101 mechanistic hypotheses that are unaccessible in conventional *in vivo* studies, where the correlation
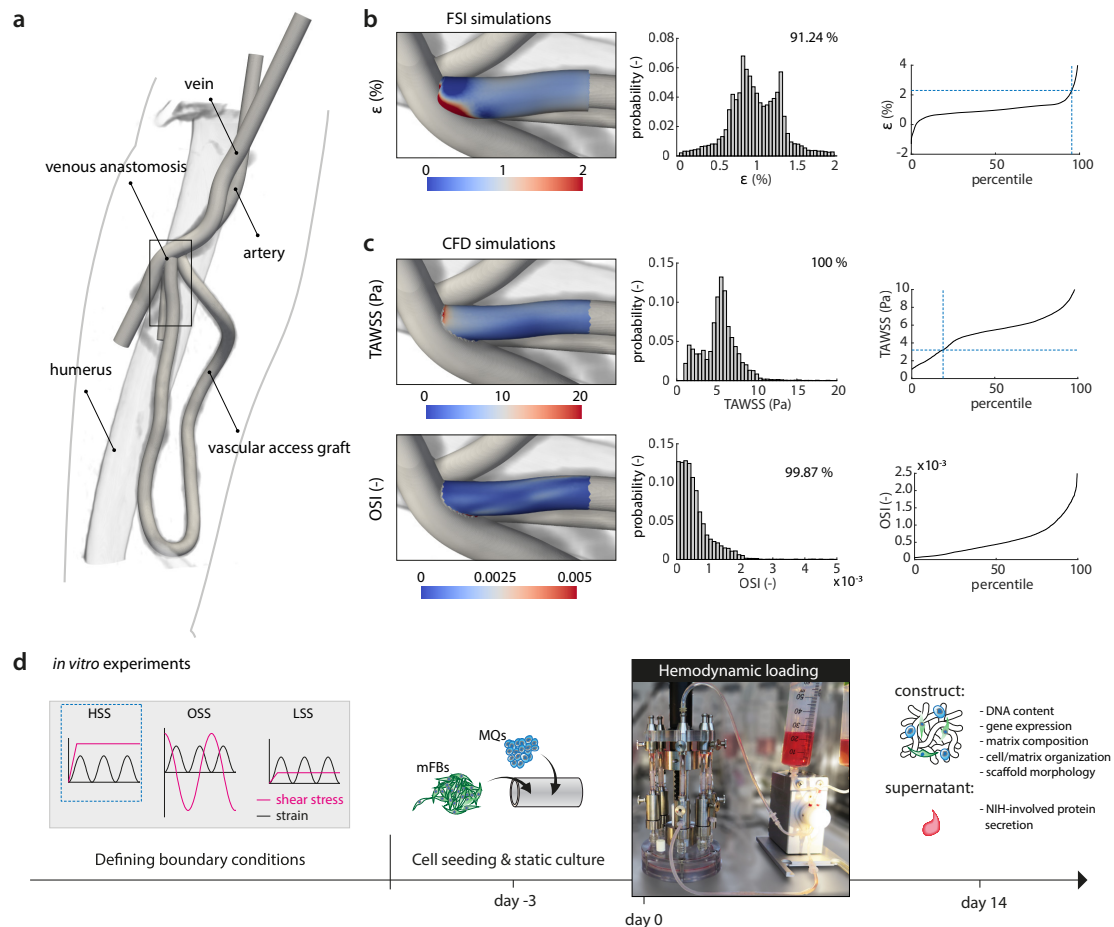
FIGURE 1. **Computational characterization of the biomechanical environment in an AVG as input for scaffold-driven neotissue formation *in vitro*. (a)** Geometry of the arteriovenous graft (AVG), looped between the axillary artery and axillary vein, that was used for the computational model (humerus inserted as a reference, venous anastomotic region indicated by *rectangle*). **(b)** Fluid structure interaction (FSI) simulations and **(c)** computational fluid dynamics (CFD) simulations to compute the local strains and shear stresses in the AVG, respectively (histograms and associated percentile plots showing the distribution of the quantified read-out parameters (ε, strain; TAWSS, time-averaged wall shear stress; OSI, oscillatory shear index). The *dashed lines* in the percentile plots correspond to the boundary conditions of the high shear stress (HSS) group in the *in vitro* experiments). **(d)** The computational results guide the *in vitro* experiments by defining the relevant boundary conditions (HSS, high shear stress; OSS, oscillating shear stress; LSS, low shear stress). (Myo)fibroblasts (mFBs) and PMA-stimulated THP-1 cells (macrophages, MQs) are co-seeded in the scaffolds using fibrin. After 3 days of static culture, the constructs are exposed to HSS, OSS, or LSS during 14 days, all in the presence of strain. After the dynamic culture, constructs and supernatants are collected and processed for further analysis.

102 between local hemodynamics, derived from computational models, and tissue composition, derived
103 from histological stainings, is indirect and often only qualitative [10].

104   A selection of the computed hemodynamic parameters at the vein-graft anastomosis, represent-
105 ing a single snapshot of the spatiotemporal hemodynamic profile in this venous perianastomotic
106 region, served as boundary conditions of the *in vitro* experiments (Fig. 1d). We selected a biome-
107 chanical condition that falls between the 15th and 100th percentiles of the strain and shear stress
108 datasets (blue dotted lines in Fig. 1b ($\sim 2\%$), c (~ 3 Pa)), referred to as the HSS (high shear stress)
109 condition. Given the hypothesis that shear stress is the driving factor of NIH, we selected one other
110 shear stress metric that is proposed to correlate with NIH: oscillating shear stress (OSS, ± 3 Pa).
111 To test the effects of HSS and OSS on neotissue development and NIH-involved protein secretion
112 in our *in vitro* model of scaffold-guided vascular growth, we compared against a physiological low
113 shear stress (LSS, ~ 0.5 Pa) control, as described by Malek *et al.* [20].

114   The *in vitro* model consists of a cell-laden tubular scaffold construct mounted around imperme-
115 able silicone tubing and centered in a glass tube in a multi-cue bioreactor. The resulting annular
116 channel is perfused with medium at a constant pressure gradient to apply laminar shear stress (in
117 the HSS and LSS groups), or at an 1 Hz alternating pressure gradient to apply oscillatory shear
118 stress (in the OSS group). The silicone tubing is cyclically pressurized up to a constant pressure
119 at 1 Hz to apply circumferential stretch. For detailed description of the bioreactor, the reader is
120 referred to our earlier work [21, 22].

121 **The biomechanical environment during *in vitro* culture.** The vascular scaffolds for the
122 *in vitro* experiments, with a wall thickness of 200 μm and inner diameter of 3 mm, were pro-
123 duced using electrospinning from poly(ε-caprolactone) bis-urea (PCL-BU, Fig. 2a). This polymer
124 is soft, tough, biodegradable, and easy to functionalize, and therefore an attractive biomaterial
125 for *in situ* TE [23]. The resulting scaffolds, with a Young's Modulus of 3 MPa [15], exhibited an
126 isotropic microstructure with ~ 5 μm fiber diameter, which remained stable during the course of
127 the culture, independent of the applied loading condition (Fig. 2b, c).

128   To mimic the early phase of the *in situ* scaffold environment, scaffolds were seeded with a
129 2:1 mixture of human THP-1-derived macrophages and primary vascular-derived (myo)fibroblasts
130 using fibrin as a cell carrier. Following 3 days of static culture, the cell-seeded constructs were cul-
131 tured for 14 days in Xanthan Gum (XG)-enriched medium containing L-ascorbic acid 2-phosphate
132 (AA2P) under various shear stress conditions in the presence of low cyclic circumferential strain
133 ($2.3 \pm 0.4\%$ at 1 Hz, Fig. 2d), mimicking the predicted strain values in AVGs as computed by the
134 FSI simulations (Fig. 1b). XG was added to match medium viscosity to blood viscosity (about
135 $4 \cdot 10^{-3}$ Pa·s for a wall shear rate of $\sim 200\,\text{s}^{-1}$ [24]), while AA2P was added to stimulate matrix
136 formation [25]. Rheology measurements indicated that the viscosity of the XG-enriched medium
137 was approximately 2.5-fold higher compared to that of standard medium, confirming that medium
138 viscosity was increased toward the range of blood viscosity (Fig. 2e) [24].

139   Samples in the HSS and OSS conditions were exposed to a maximum shear rate of $1216 \pm 128\,\text{s}^{-1}$,
140 and samples in the LSS condition to $93 \pm 31\,\text{s}^{-1}$ (left panels in Fig. 2f, g). The applied strains and
141 shear rates were successfully maintained over the complete culture period, except at day 4 in the
142 LSS condition where the shear rate dropped slightly to $\approx 60\,\text{s}^{-1}$ (left panel in Fig. 2g). Using the
143 quantified viscosity of the XG-enriched medium, the shear rate applied to the samples translated
144 to a shear stress of ($\pm$) 3.2 ± 0.1 Pa for the HSS (unidirectional) and OSS (complete flow reversal)
145 condition (right panel in Fig. 2f), of which the magnitude is within the range of expected shear
146 stress values in AVGs as computed by the CFD simulations (Fig. 1c). For the LSS condition, this
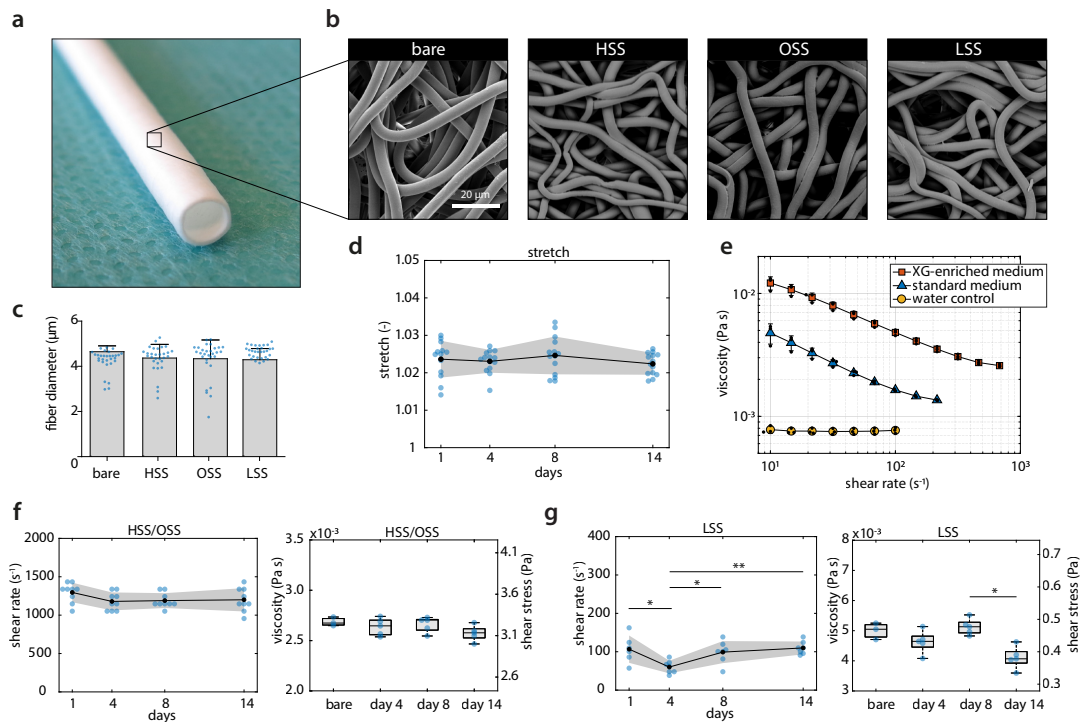147 translated to 0.44 ± 0.05 Pa (right panel in Fig. 2g), which is within the range of 0.1 Pa–0.6 Pa in

FIGURE 2. *In vitro* **modeling of scaffold-guided vascular growth.** **(a)** Electrospun PCL-BU vascular scaffold prior to culture ($\varnothing 3\,\mathrm{mm}$). **(b)** Scanning electron microscopy images of dynamically cultured samples after decellularization for each experimental condition, and of an 8-day statically cultured cell-free sample (bare). **(c)** Quantification of scaffold fiber diameter at the outside of the (decellularized) constructs ($n = 30$ fibers/condition). **(d)** Temporal variations in cyclic stretch for all loading conditions ($n = 13$–14/day). **(e)** Shear-rate dependent viscosity in XG-enriched medium (*red squares*, $n = 3$), standard medium (*blue triangles*, $n = 3$), and water (*yellow circles*, $n = 3$). **(f, g)** Temporal variations in shear rate (*left*, $n = 6$–9/day), viscosity (*right*, $n = 3$ for bare medium sample, $n = 5$/day), and shear stress (*right axis*, derived from the actual (measured) medium viscosity) in the high, oscillating, and low shear stress conditions. Bars and points represent mean, error bars and gray area indicate standard deviation, boxplots contain $50\,\%$ of the data with median highlighted by central mark (* $p < 0.05$, ** $p < 0.01$).

healthy veins [20]. The applied shear stresses remained stable over time, except for a small drop in the LSS condition at day 14 (Fig. 2g, $p = 0.0102$).

These results demonstrate that we were able to keep the biomechanical cellular environment, in terms of passive cues (via the scaffold fibers) and active cues (via the shear stresses and strains), stable and at the required level. This precise experimental control allowed us to directly correlate the biological response to the applied loading regime.

Oscillatory shear stress activates macrophages and myofibroblasts. Using this dynamic *in vitro* setup, we quantified the cell and tissue growth and characterized the phenotypes of the cells in response to the different types of shear stress. The dynamic co-culture led to an overall increase of the construct mass with time, especially for the samples exposed to HSS and OSS (Fig. 3a). At day 14, scaffolds were completely populated with cells in all conditions and an increasing, but non-significant ($p = 0.143$), trend of cell content with high (81 %) and oscillating shear stress (118 %) compared to LSS was observed (Fig. 3b). However, the variation in DNA content within the groups was large, and no clear difference between the appearance and proliferative state of cells could be observed (Fig. 3c, d).

The appositional cell/matrix layer (i.e., the side that was exposed to the flow) aligned in the direction parallel to the flow (Fig. 3e). This layer contained elongated cells with stress fibers (top row in Fig. 3f). At the other side of the scaffold, cells with a more rounded morphology were observed (bottom row in Fig. 3f). Elongated cells stained positive for vimentin, indicating that the outside of the constructs was populated primarily by the (myo)fibroblasts (Fig. 4a). CD45, as an indicator of the macrophages, was mostly found in the middle layers of the constructs and to a lesser extent compared to vimentin. This was to be expected as a result of (myo)fibroblast proliferation and a possible reduction in macrophage number (e.g., as a result of apoptosis and transdifferentiation).

Previously, it has been shown *in vivo* that OSS ($\approx$14 Pa; range of 60 Pa) induces smooth muscle cell-rich plaque-formation, while LSS ($\approx$10 Pa) induces the occurrence of M1-polarized macrophage-rich plaques in the carotid artery in mice [26, 27, 28]. Note that the seemingly large discrepancy between these magnitudes of wall shear stress and the definition of 'low shear stress' we used in this study is attributable to the known inverse relationship between animal size and wall shear stress [29]. To test whether different biomechanical environments can indeed influence macrophage polarization, we examined the relative expression of M1 and M2 macrophage markers at HSS and OSS compared to LSS. Interestingly, we did not detect a polarization toward an M1 or M2 macrophage phenotype (Fig. 4b). Only CD68 (pan-macrophage marker) and IL10 (anti-inflammatory marker) were more clearly activated with OSS ($p = 0.0216$ and $p = 0.1224$, respectively), and to a lesser extent with HSS ($p = 0.1819$ and $p = 0.6740$, respectively, Fig. 4c). Similar to the dualistic macrophage phenotype, the phenotype of the (myo)fibroblasts could not be uniquely attributed to be either synthetic or contractile. Instead, we found simultaneous upregulation of S100A4 (synthetic marker) and smoothelin (contractile marker), and downregulation of calponin (contractile marker) with OSS ($p = 0.0350$, $p = 0.0082$, and $p > 0.9999$, respectively) and HSS ($p = 0.1024$, $p = 0.8686$, and $p = 0.1096$, respectively, Fig. 4c).

Contrary to the gene level analysis of MCP-1 ($p = 0.0075$), TNF-α ($p = 0.2423$), and IL-6 ($p = 0.1763$), at the protein level these cytokines were lower expressed in the OSS-group compared to the LSS-group, although the variation within each group was large (Fig. SIIIb). With respect to growth factors (TGF-β1 ($p = 0.1203$), CTGF ($p = 0.9973$)) and proteinases (MMP-1 ($p = 0.0122$), MMP-9 ($p = 0.0378$), TIMP-1 ($p = 0.0075$)), similar trends as seen for the cytokines were observed, which were significant for the proteinases, but not for the growth factors (Fig. SIIIb). However, this quantification only represents a single snapshot in time, while protein and RNA expressions are typically highly dynamic in nature. In addition, the discrepancy between gene and protein secretion could indicate that the translation from RNA to protein is differently regulated, or that the protein stability in the culture medium is reduced in HSS- and OSS-conditions [30].

Together, the results suggest that OSS activates (myo)fibroblasts and macrophages to grow new tissue in terms of both cell number and matrix. Moreover, the reduction of proteinase secretion in
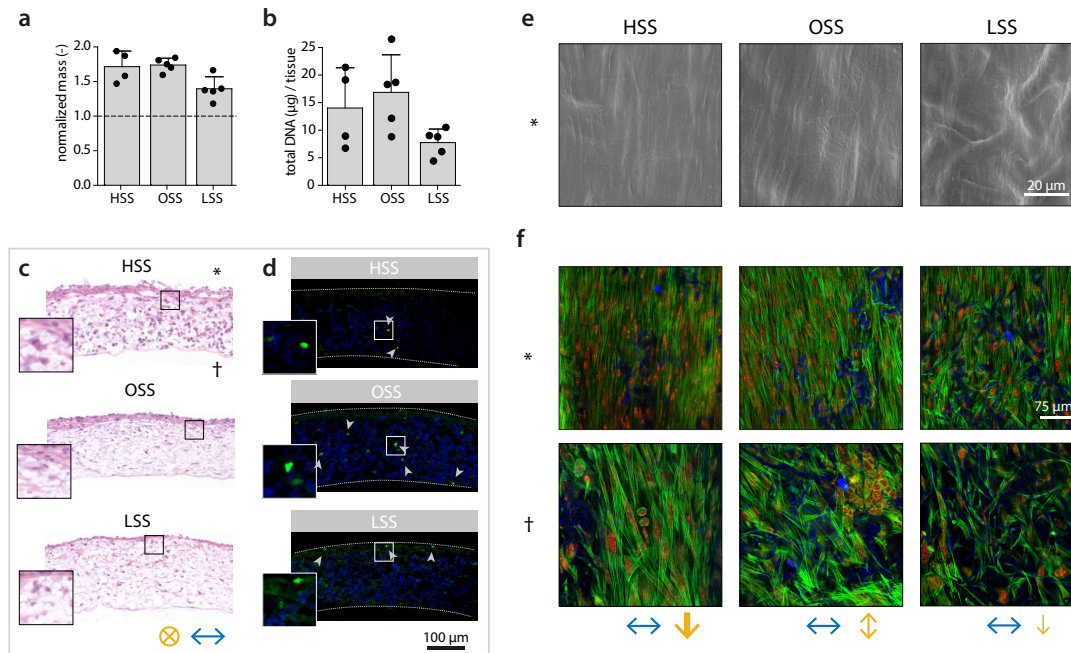
FIGURE 3. **Cell and tissue growth at day 14 under different types of shear stress. (a)** Overall construct mass/surface at day 14 normalized to scaffold mass/surface prior to seeding (*dashed line* indicates no change). **(b)** Total DNA content per tissue construct. **(c)** Hematoxylin and eosin-stained cross-sections. **(d)** Localization of Ki67-positive cells (Ki67 in *green*, scaffold material in *blue*, *dashed lines* indicate construct borders). **(e)** Scanning electron microscope image of the cell and tissue morphology. **(f)** In-plane visualization of the F-actin cytoskeleton (actin in *green*, nuclei in *red*, and scaffold fibers in *blue*). Bars represent mean ± standard deviation. ∗, side exposed to flow; †, inside of the construct. Flow directions indicated by *yellow arrows* (magnitude indicated by arrow thickness) and stretch directions indicated by *blue arrows*. HSS, high shear stress condition (3.2 Pa, $n = 4$); OSS, oscillatory shear stress condition (±3.2 Pa, $n = 5$); LSS, low shear stress condition (0.4 Pa, $n = 5$).

the OSS-group suggests a suppressed tissue-remodeling environment, favoring neotissue formation rather than tissue degradation.

Oscillatory shear stress promotes disorganized tissue growth. Next, we sought to investigate the effect of the different shear stress metrics on tissue formation and remodeling. Overall, the gene expression of all growth and remodeling markers, with the exception of TGFB1, was (non-significantly) elevated with OSS compared to HSS (Fig. 5a). The expression of collagen type I/III, decorin, versican, fibrillin 1, MMP1, MMP2, and TIMP1/2 was also higher compared to the LSS-condition, which was statistically significant for decorin ($p = 0.0385$) and MMP1 ($p = 0.0122$). Interestingly, the trends of MMP9 and TGFB1 are similar to the trends at the protein level
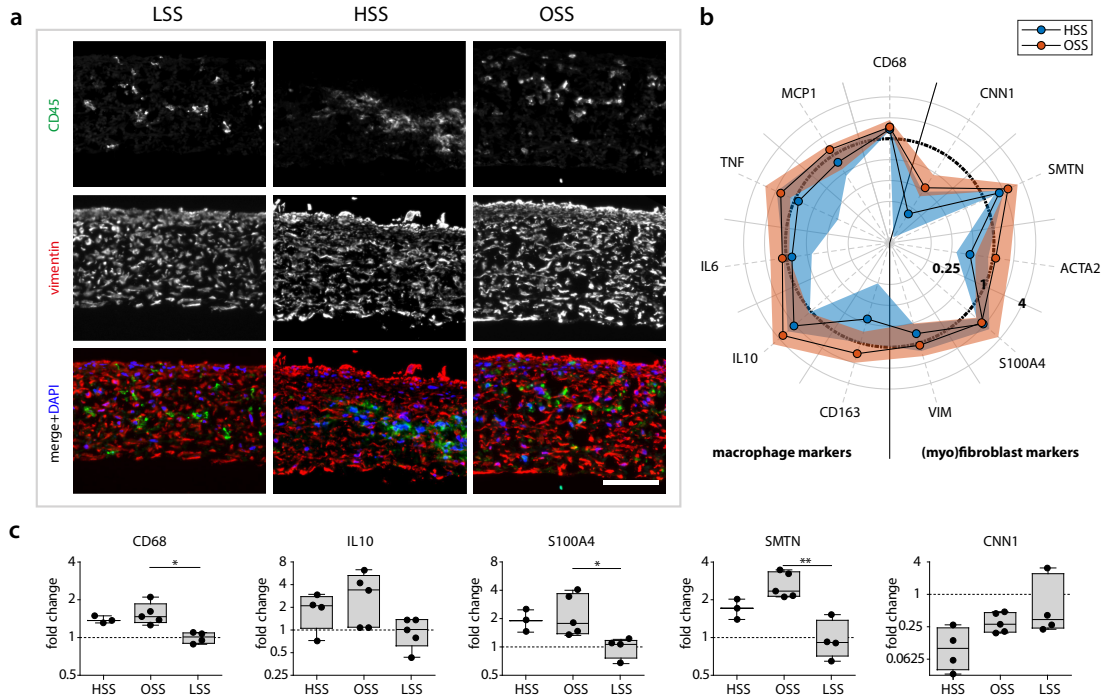
FIGURE 4. **Phenotypical characterization of the cells in the vascular constructs at day 14. (a)** Representative cross-sections for each experimental group stained for CD45 (*green*) and vimentin (*red*) for the localization of macrophages and (myo)fibroblasts, respectively (nuclei are indicated in the *lower panel* in *blue*). **(b)** Relative gene expression compared to the low shear stress condition (indicated by the *circle* at 1) for macrophage-related genes (*left part* of the polar plot) and (myo)fibroblast-related genes (*right part* of the polar plot, $n \geq 3$/group). The *dots* and *shaded areas* indicate, respectively, the 50th and 25th–75th percentiles. **(c)** Boxplots for a selection of phenotypical-related genes ($n = 3$–5, * $p < 0.05$, ** $p < 0.01$). Boxplots contain 50% of the data with median highlighted by central mark. HSS, high shear stress condition (3.2 Pa); OSS, oscillatory shear stress condition (± 3.2 Pa); LSS, low shear stress condition (0.4 Pa). See Fig. SIV for all boxplots of the gene expression data.

209 (Fig. SIIIb), while MMP1 and TIMP1 follow an opposite trend, suggesting different mechanisms
210 that regulate RNA to protein translation.
211   Collagen staining and HYP quantification revealed that, compared to unidirectional shear stress
212 (i.e., LSS and HSS), OSS stimulated the synthesis of more and thicker collagen fibers (Fig. 5b, d).
213 These fibers are especially suited to resist *in vivo* loading and slowly take over the load-bearing
214 properties of the resorbing scaffold. However, this process can result in scar-like tissue if collagen
215 production happens too fast. HSS stimulated relatively more collagen type I formation while α-
216 SMA-positive cells were predominantly detected at the tissue borders with LSS (Fig. 5c). These
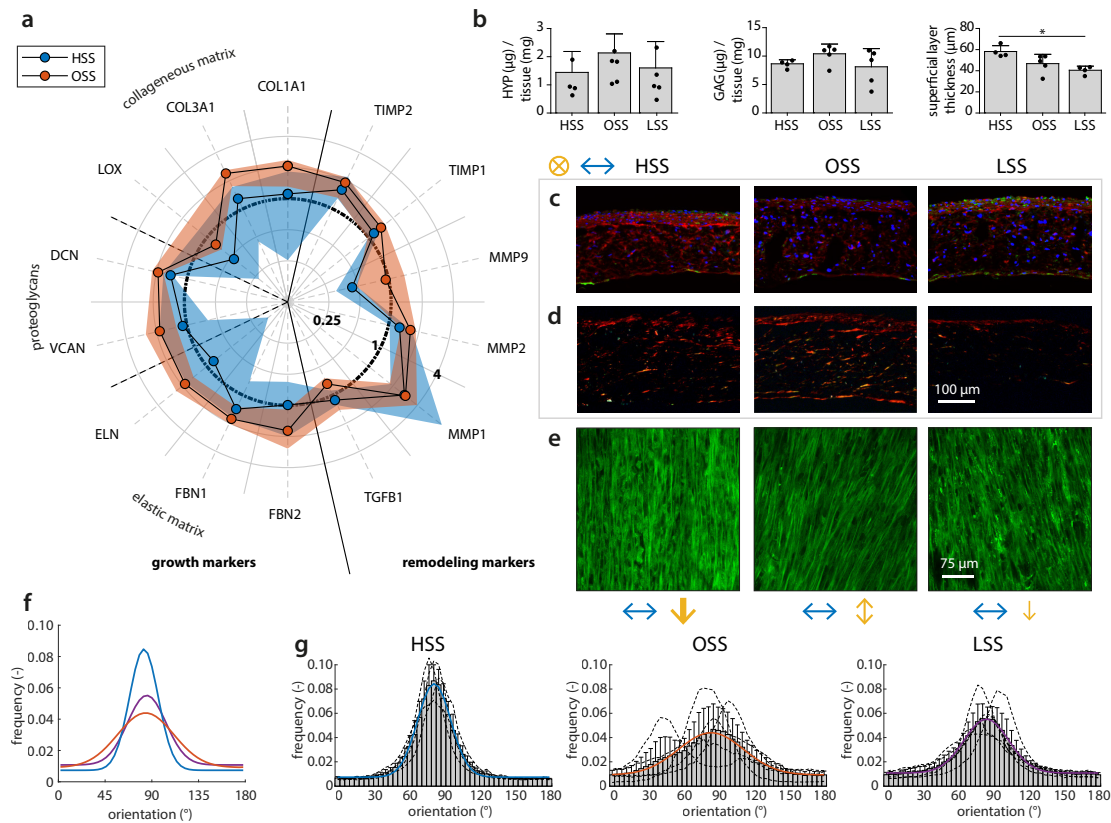
FIGURE 5. **Changes to matrix growth, remodeling, and organization in response to shear stress.** **(a)** Relative gene expression compared to the low shear stress condition (indicated by the *circle* at 1) for markers related to growth (i.e., collageneous matrix, proteoglycan, and elastic matrix formation), as well as markers related to remodeling. The *dots* and *shaded areas* indicate, respectively, the 50th and 25th–75th percentiles. See Fig. SIV for all boxplots of the gene expression data. **(b)** Total hydroxyproline (*left*) and glycosaminoglycan (*middle*) content normalized to total construct mass, and quantification of the thickness of the appositional collagen layer on top of the scaffold from the confocal z-stacks in **(e)** (*right*, * $p < 0.05$). Representative sections of each experimental group stained for **(c)** αSMA (*green*), collagen I (*red*), and DAPI (*blue*) and **(d)** Picrosirius red (visualized under polarized light). **(e)** Confocal visualization of the collagen structure. **(f)** Overlay plot and **(g)** separate histograms quantifying the angular collagen distribution in the appositional matrix layer for each condition (directions of applied shear stress (90°) and stretch (0°) indicated by the arrows in **(c, d)** and **(e)**). Bars represent mean $\pm$ standard deviation. HSS, high shear stress condition (3.2 Pa, $n = 4$); OSS, oscillatory shear stress condition ($\pm$3.2 Pa, $n = 5$); LSS, low shear stress condition (0.4 Pa, $n = 4$–5).

217 observations are in line with the increased expression of growth markers at the gene level (Fig. 5a)
218 and may have been further stimulated by the decreased levels of proteinases in the culture medium
219 (Fig. SIIIb).
220   We then focused on the neotissue organization in the appositional tissue layer which was in direct
221 exposure to the shear stress and whose thickness was highest with HSS ($p = 0.0205$ compared to
222 LSS, Fig. 5b, e). The collagen fibers were mainly oriented at an angle between 80° and 90° in all
223 groups (i.e., parallel to the flow direction), and compared to LSS, consistently more aligned in
224 the HSS-condition, despite the limited differences in proteinase secretion (Fig. SIIIb). In contrast,
225 the peak in the OSS-condition was much broader compared to LSS and HSS, indicating that the
226 collagen is deposited with a substantially higher in-plane fiber dispersion when the flow is not
227 unidirectionally applied. Based on these findings, we conclude that the collagen fiber dispersion in
228 the superficial collagen layer is a direct result of flow-induced shear stress, rather than an indirect
229 result of the secreted proteinases. On the other hand, the overall collagen fiber orientation is not
230 necessarily mediated by shear stress alone, as the presence of cyclic strain has also contributed to
231 this fiber orientation [15].
232   In addition to tissue growth and remodeling by the (myo)fibroblasts, we aimed at scaffold
233 degradation that is mainly induced by the macrophages. As the macrophages resided in the center
234 of the scaffold and not at the surface, prohibiting the assessment of scaffold degradation by SEM,
235 we examined the expression of genetic markers responsible for scaffold degradation. In the OSS-
236 group, NFKB1 (a protein complex involved in oxidative stress) was upregulated compared to LSS
237 (Fig. SII, $p = 0.0044$). LIPA (lysosomal lipase) followed a similar trend. On the other hand, NOX2
238 (ROS generating NADPH Oxidase 2 complex), which is involved in oxidative degradation, followed
239 a decreasing, albeit non-significant, trend in the HSS-condition.
240   Although this could indicate enhanced oxidative and enzymatic degradative capacity of the
241 macrophages with OSS, a previous study showed that the expression of these genes could not
242 explain the differences in macrophage-driven scaffold mass loss, making it difficult to directly
243 relate gene expression to scaffold degradation [31, 32]. In the future, the analysis should therefore
244 be extended with, for example, Raman spectroscopy on cross-sections, allowing the assessment of
245 scaffold degradation across the thickness of the constructs [33].

246   CONCLUSIONS AND OUTLOOK (354 WORDS)

247   This study aimed to elucidate how neotissue develops under the influence of the hemodynamic
248 environment in regenerating AVGs via a combined *in silico* and *in vitro* approach (Scheme 1).
249 With this approach, the hemodynamic environment could be controlled in a systematic way and
250 biological responses could be directly measured, allowing the identification of causal relationships
251 between hemodynamic parameters and the venous remodeling process. Relevant hemodynamic
252 parameters were selected according to currently existing theories on venous remodeling (i.e., oscil-
253 latory shear stress and high shear stress [11]), while the exact magnitudes were derived from CFD
254 and FSI simulations (Scheme 1a, b).
255   Using these *in vitro* dynamic co-cultures, we demonstrated that, compared to unidirectional
256 shear stress (i.e., LSS and HSS), OSS activates both cell types to grow and remodel a tissue with a
257 dense and disorganized structure (Scheme 1c). Furthermore, the secretion of NIH-related proteins
258 was lower in the OSS- and HSS-condition, indicating that the interaction between the different
259 cell types and their mechanical environment resulted in a microenvironment that likely favored
260 neotissue formation rather than tissue degradation. Here, it should be noted that other (complex)
261 shear stress theories exist as well (e.g., spatial and/or temporal gradients in shear stress [11]),

262 and that the cellular composition and phenotypes may differ in patients requiring vascular access,
263 which should be the subject of future investigation.

264   Taken together, we identified oscillatory shear stress as a moderate, but progressive stimulator
265 of cell proliferation and neotissue formation, even in the presence of cyclic strain. This is remark-
266 able, because it was previously shown that laminar shear stress can have a stabilizing effect on
267 strain-induced neotissue formation [15], making oscillatory shear stress a potential target to inhibit
268 venous NIH and avoid excessive tissue formation. In the future, integration of these findings on
269 cell mechano-response in the presence of complex hemodynamic situations into a computational
270 framework of growth and remodeling can lead to the exciting possibility to predict the scaffold
271 and venous (mal)adaptation to altered hemodynamics [34, 35]. A thorough understanding of these
272 mechanisms is essential to successfully translate *in situ* TE into a therapeutic approach as a solu-
273 tion to reduce vascular access dysfunction in patients with end-stage renal disease.

274

275 title characters: 126 / 130
276 abstract word count: 167 / 175
277 main text word count: 3500 / 3500
278 methods word count: 2636 / 3000
279 display items: 6/8
280 references: 44/50

281   METHODS (2636 WORDS)

282 **AVG geometry reconstruction.** Realistic axillary-artery to axillary-vein loop AVG geometries were used as
283 input for the CFD and FSI models. These geometries were reconstructed using clinical data of a single patient and
284 assumed constant-diameter vessels. For the CFD AVG model, vessel paths and AVG configuration were assumed
285 to remain relatively constant after AVG creation. As such, these AVG characteristics were extracted from a 15-
286 month postoperative CTA scan by means of vessel-centerline extraction. Since vessel diameters may have changed
287 significantly in the period between AVG creation and the CTA scan, 2-weeks preoperative ultrasound diameter
288 measurements were used to estimate arterial and venous diameters (6.6 mm and 7.7 mm, respectively). Graft
289 diameter was set to 6 mm. For the FSI model a similar approach was taken, though for this model zero-pressure vessel
290 diameters needed to be imposed. The zero-pressure venous diameter was set to 7.1 mm, which was approximated
291 using estimates of the average blood pressure at the time of ultrasound diameter measurements [1]. Zero-pressure
292 graft diameter was set to 6 mm.

293 **Simulations.** The CFD equations were solved by using the OASIS [36] solver as implemented in the open-source
294 finite element package FEniCS [37]. A mesh-independent solution was obtained at $3.1 \cdot 10^6$ tetrahedral Taylor-Hood
295 elements and a time step of $1 \cdot 10^{-4}$ s. The FSI model was solved by using the Unicorn [38] solver that was also
296 implemented in FEniCS. A mesh-independent solution was obtained at $2.5 \cdot 10^6$ and $0.6 \cdot 10^6$ linear tetrahedral
297 elements in the fluid and solid domain, respectively. Blood was modeled as Newtonian fluid with a kinematic
298 viscosity of $3.3 \cdot 10^{-6}$ m$^2 \cdot$s^{-2} for the CFD simulations and $4.5 \cdot 10^{-6}$ m$^2 \cdot$s^{-2} for the FSI simulations. From the CFD
299 simulations, exposure to wall shear stress in the perianastomotic region was quantified using the time averaged wall
300 shear stress magnitude (TAWSS):

$$(0.1) \qquad \mathrm{TAWSS} = \frac{1}{\mathrm{T}} \int_0^{\mathrm{T}} ||\vec{\tau}(t, \vec{x})|| \mathrm{dt}$$

301 where $\vec{\tau}(t, \vec{x})$ represents the local WSS vector and T the duration of the cardiac cycle. Exposure to oscillatory wall
302 shear stress was assessed using the oscillatory wall shear stress index (OSI):

$$(0.2) \qquad \mathrm{OSI} = \frac{1}{2} \left(1 - \frac{|| \int_0^{\mathrm{T}} \vec{\tau}(t, \vec{x}) \mathrm{dt}||}{\int_0^{\mathrm{T}} ||\vec{\tau}(t, \vec{x})|| \mathrm{dt}} \right)$$

303 which ranges between 0 (unidirectional WSS) and 0.5 (purely oscillatory WSS). From the FSI simulations, wall
304 strain was computed over the inner and outer surface of the graft wall according to:

$$(0.3) \qquad \varepsilon = \sqrt{\frac{A_\mathrm{n} - A_0}{A_0}}$$

305 Here, A_0 is the initial area of each surface element on the graft wall, whereas A_n is the surface area of each element
306 during the cardiac cycle. Finally, ε was averaged over the complete cardiac cycle. The ε strain metric is equivalent to
307 engineering strain and combines both longitudinal and circumferential strain in a single scalar metric. For detailed
308 information regarding the methodology of the simulations, the reader is referred to Quicken *et al.* [17, 1].

309 **Scaffold preparation.** Tubular scaffolds ($\varnothing$3mm, 2 cm in length, 200 μm wall thickness) were electrospun from
310 poly(ε-caprolactone) bis-urea (PCL-BU; SyMO-Chem, Eindhoven, The Netherlands) in a climate-controlled cabinet
311 (25 °C and 30 % relative humidity; IME Technologies, Geldrop, The Netherlands). Briefly, 15 % (w/w) PCL-BU
312 was dissolved in 85 % (w/w) CHCl$_3$ (Sigma, 372978) and delivered via a charged nozzle (-1 kV) at a flow rate
313 of 40 μl·min^{-1} onto a positively charged (16 kV) rotating cylindrical mandrel ($\varnothing$3 mm, 500 rpm). The distance
314 between the nozzle and the mandrel was kept constant at 16 cm. The resulting scaffolds were removed from the
315 mandrel, dried *in vacuo* overnight, and placed over silicone tubing ($\varnothing$2.8 mm). The scaffold-wrapped silicone tubing
316 was mounted in the bioreactor, sterilized by UV exposure (30 min/side), wetted in sterile H$_2$O, and incubated at
317 37 °C in complete medium (1:1 advanced Dulbecco's modified Eagle Medium (a-DMEM):Roswell Park Memorial
318 Institute 1640 (RPMI-1640) (Gibco, 124910 and A10491) with 10 % fetal bovine serum (FBS; Greiner, Alphen aan
319 den Rijn, The Netherlands), 1 % penicillin/streptomycin (P/S; Lonza, DE17-602E), 0.5 % GlutaMax (Gibco, 35050),
320 and 0.25 mg·ml^{-1} L-ascorbic acid 2-phosphate (AA2P, Sigma, A8960)) overnight to allow for protein adsorption.

321 **(Myo)fibroblast cell culture.** Vascular cells were isolated from surgical leftover of human vena saphena magna
322 and used in accordance to the Dutch guidelines for secondary-use materials. The cells were expanded conforming
323 conventional protocols [39]. Due to their structural properties, these cells have earlier been characterized as my-
324 ofibroblasts [39, 40]. However, a subpopulation of these cells do not express α-SMA, which is more characteristic
325 for fibroblasts [40]. Therefore, we refer to these cells as (myo)fibroblasts (mFBs). mFBs were cultured in a-DMEM
326 containing 10 % FBS, 1 % P/S, and 1 % GlutaMax in a standard culture incubator (37 °C, 5 % CO$_2$) and passaged
327 at 80 % confluency. Culture medium was changed every 3–4 days.

328 **THP-1 cell culture.** Human monocytic THP-1 cells (Sigma Aldrich, lot# 16K052) were cultured and expanded
329 in suspension at a cell density of (0.5–1.5)·10^6 cells·ml^{-1} culture medium (RPMI-1640 containing 10 % FBS and
330 1 % P/S) in a standard culture incubator (37 °C, 5 % CO$_2$). Culture medium was changed three times per week.

331 **Cell seeding.** After cell expansion, the mFBs (passage 6) and THP-1 cells (passage 10 after thawing) were seeded
332 in the pre-wetted scaffolds using fibrin as a cell carrier [41]. Prior to seeding, the THP-1 cells were primed for 15
333 min in 50 ng·ml^{-1} phorbol 12-myristate 13-acetate (PMA; Sigma, P8139)-enriched culture medium to stimulate
334 macrophage differentiation. To co-seed the cells into the porous scaffold, cells (15·10^6 mFBs·cm^{-3} and 30·10^6 THP-
335 1 cells·cm^{-3}) were added to a mixture of bovine fibrinogen (10 mg·ml^{-1}; Sigma, F8630) and bovine thrombin (10
336 IU·ml^{-1}; Sigma, T4648), and carefully pipetted onto the scaffold. To complete fibrin polymerization, the cell-seeded
337 constructs were transferred to a 15 ml tube and kept in an incubator (37 °C, 5 % CO$_2$) for 30 min, after which the
338 tubes were filled with 8 ml of complete medium. To allow for cell adhesion to the scaffold fibers, the constructs were
339 statically cultured in these tubes for 3 days prior to exposing the constructs to the different hemodynamic loading
340 conditions (Fig. 1d).

341 **Shear stress and strain application.** After 3 days of static culture, the constructs were mounted in the culture
342 chambers of the bioreactor for the application of hemodynamic loading as previously described [21]. To determine
343 the loading conditions that mimic the conditions *in vivo*, we first examined the expected hemodynamic loads
344 at the vein-graft anastomosis, as computed from the computational fluid dynamic and fluid-structure interaction
345 simulations [17, 1]. To each loading condition, $n = 5$ constructs were assigned to allow for statistical analysis. The
346 medium reservoirs were filled with 50 ml of complete medium, which was supplemented with 0.7 mg·ml^{-1} xanthan
347 gum (XG; Sigma, G1253) to increase the medium viscosity towards the range of blood viscosity [24]. To correct for
348 possible medium evaporation during culture, the culture medium was supplemented up to 50 ml with sterile H$_2$O
349 every 4 days, after which 25 ml of medium was replaced by fresh, XG-supplemented complete medium. After 14 days
350 of dynamic culture, the tubular constructs were harvested, sectioned according to a cutting scheme (Fig. SI), and
351 stored at 4 °C (after 15 min fixing in 3.7 % formaldehyde and 3×5 min washing in PBS) or -30 °C (after snap-freezing

352 in liquid nitrogen) until further analysis. Supernatants from the culture medium after centrifugation (300 g, 5 min)
353 at day 1, 4, 8, and 14 were stored at -30 °C until further analysis.

354 **Xanthan gum sterilization and dissolving.** In a sterile environment, XG was spread on a weighing paper
355 in a large petri dish and UV-sterilized (10 min on two sides). After UV-exposure, the XG was transferred to a
356 pre-weighed 50 ml tube, and weighed again to determine the XG mass in a sterile way. Then, 70 % EtOH was
357 added at a concentration of $1.4 \, \mu l \cdot mg^{-1}$ XG and the resulting suspension was transferred to 1:1 a-DMEM:RPMI-
358 1640 at a concentration of $1.4 \, mg \cdot ml^{-1}$. The sterilized XG was dissolved on a magnetic hot plate stirrer (4 h at
359 40 °C), resulting in a viscous solution. To prepare the XG-supplemented complete medium, this viscous solution
360 was diluted $2 \times$ with 1:1 a-DMEM:RPMI-1640 to which the rest of the supplements were added (10 % FBS, 1 %
361 P/S, $0.25 \, mg \cdot ml^{-1}$ AA2P).

362 **Viscosity measurements.** To determine the shear stresses associated with the applied shear rates during the
363 experiment, the viscous behavior of the supernatants (with and without XG) was quantified using a cone-plate
364 rheometer ($\varnothing 50$ mm) at 37 °C (ARES, Rheometric Scientific). The viscosity η was measured at shear rates $\dot{\gamma}$
365 varying from $10 \, s^{-1}$ until $1500 \, s^{-1}$ (6 measurements per decade). The resulting viscosity-shear rate curves were
366 linearly interpolated to determine the viscosities at low shear rate ($\dot{\gamma} \approx 100 \, s^{-1}$) and high shear rate ($\dot{\gamma} \approx 1200 \, s^{-1}$)
367 (Matlab, The Mathworks, Natick, MA). The shear stress was calculated via: $\tau(\dot{\gamma}) = \dot{\gamma} \cdot \eta(\dot{\gamma})$.

368 **Biochemical assays.** The snap-frozen samples were used for quantification of DNA, glycosaminoglycan (GAG),
369 and hydroxyproline (HYP) content. After determination of the sample dry mass and surface (see Determination of
370 total mass), samples were reduced to a fine powder using a micro-dismembrator (Sartorius) for sample digestion.
371 Briefly, the samples were placed in cryovials containing 4 microbeads, frozen in liquid nitrogen, and disrupted at
372 3000 rpm for 60 s. To digest the sample, the powder was mixed with 500 μl digestion buffer (100 mM phosphate
373 buffer (pH=6.5), 5 mM L-cysteine (C-1276), 5 mM ethylene-di-amine-tetra-acetic acid (EDTA, ED2SS), $140 \, \mu g \cdot ml^{-1}$
374 papain (P4762); all from Sigma), transferred to a fresh Eppendorf tube, and incubated overnight at 60 °C. Prior to
375 measurement of DNA, GAG, and HYP content, the samples were centrifuged at 12,000 rpm for 10 min. From the
376 supernatant, DNA was quantified using the Qubit dsDNA BR assay kit (Life Technologies, Q32853) according to
377 the manufacturer's protocol. GAG was quantified using a modified dimethyl methylene blue (DMMB) assay [42]
378 with Shark chondroitin sulfate (Sigma, C4348) as a standard. Briefly, 40 μl of the supernatant and standards were
379 mixed with 150 μl DMMB solution in a 96-well plate. The absorbance was measured using a microplate reader (540
380 nm, Synergy HTX, Biotek). HYP, as a measure of collagen, was quantified with a Chloramin-T assay [43] with
381 trans-4-hydroxyproline as a reference (Sigma, H5534). Before assaying, the samples were first hydrolyzed in 16 M
382 sodiumhydroxide (Merck, B1438798). The absorbance was measured using a microplate reader (550 nm, Synergy
383 HTX, Biotek). DNA, GAG, and HYP values were normalized to the sample dry mass. Normalized DNA was
384 multiplied by the sample total mass to obtain DNA content per sample (see Determination of total mass).

385 **Determination of total mass.** To obtain the mass/surface, samples were weighed using a digital balance (XS105
386 dual-range analytical balance, Mettler Toledo, Switzerland) and photographed together with a ruler. The surfaces
387 were measured from the photographs using ImageJ (v1.48, U.S. NIH, Bethesda, MD, USA). To estimate the increase
388 in construct mass during culture, the mass/surface of the lyophilized samples at day 14 (see Biochemical assays)
389 was normalized to the initial mass/surface prior to seeding. To estimate the total sample mass at day 14, the
390 mass/surface of the lyophilized samples was multiplied by the total surface of the samples (15 mm $\times$ 1.5π mm).

391 **Scanning electron microscopy (SEM).** Cell, tissue, and scaffold fiber morphology were assessed from SEM
392 images. The formaldehyde-fixed samples were placed in 0.25 % glutaraldehyde (1 h), dehydrated in an ordered
393 series of ethanol dilutions, and dried *in vacuo* overnight. After visualization of the cell and tissue morphology
394 in low vacuum using a 10 kV electron beam (Quanta 600F, FEI, Hillsboro, OR, USA), half of the samples were
395 decellularized in 4.6 % sodium hypochlorite (15 min), washed in H_2O (2×5 min), and dried *in vacuo* overnight to
396 visualize the scaffold fiber morphology. Together with the non-decellularized samples, samples were gold-sputtered
397 and visualized in high vacuum using a 10 kV electron beam.

398 **Immunohistochemistry.** Cross-sections (7 μm cryosections from formalin-fixed samples) were washed in PBS
399 (3×5 min), permeabilized in 0.5 % Triton-X 100 (30 min), and blocked for non-specific binding in 5 % goat serum
400 containing 1 % BSA (30 min). The sections were then incubated with primary antihuman polyclonal antibodies
401 against Ki67 (rabbit IgG, 1:200, Thermoscientific), CD45 (mouse IgG1, 1:1000, Abcam), vimentin (mouse IgM,
402 1:2000, Abcam), αSMA (rabbit IgG, 1:600, Abcam), or collagen I (mouse IgG1, 1:200, Sigma), in $10\times$ diluted block
403 solution (overnight at 4 °C). After washing in PBS (3×5 min), the sections were incubated with 1:500 secondary

404 goat antibodies labeled with Alexa-488 conjugate (antimouse IgG1 (for CD45, Molecular Probes) or antirabbit IgG
405 (for αSMA, Molecular Probes)) or Alexa-647 conjugate (antimouse IgM (for vimentin, Jackson Immunoresearch)
406 or antimouse IgG1 (for collagen I and Ki67, Molecular Probes)), in $10\times$ diluted block solution (60 min). Nuclei
407 were stained with 4',6-diamidino-2-phenylindole (DAPI; 1:500, Sigma). The stained sections were mounted in
408 mowiol (Sigma, 81381) and visualized with an inverted epifluorescent microscope (Zeiss Axiovert 200M, $20\times/0.5$
409 Plan-Neofluar lens).

410 **Fluorescence stainings.** Actin and collagen structures in formalin-fixed whole-mount samples were labeled with
411 phalloidin-Atto 488 (1:200, Sigma) and CNA35-OG488 ($1\,\mu$M, [44]), respectively. Nuclei in the actin-stained samples
412 were labeled with propidium iodide ($7\,\mu$M, Molecular Probes, P3566). The stained samples were kept in PBS and
413 visualized with a confocal laser scanning microscope (Leica TCS SP5X with a $40\times/1.1$ HCX PL Apo CS lens). The
414 collagen orientation in each sample was quantified from 2 z-stacks ($\approx$50 μm) recorded at different locations using
415 in-house developed software as described elsewhere [21].

416 **Histological analysis.** Overall matrix content and fibrillar collagen in cross-sections (7 μm cryosections from
417 formalin-fixed samples) were assessed from hematoxylin and eosin (H&E) and Picrosirius red stains, respectively.
418 Images were acquired with a bright field microscope (Zeiss Axio Observer Z1 with a $20\times/0.8$ Plan-Apochromat
419 lens). Picrosirius-stained sections were also imaged with polarized light to assess the birefringence of the collagen
420 fibrils.

421 **Gene expression.** The snap-frozen samples were disrupted in a micro-dismembrator (see Biochemical assays) and
422 lysed in RLT lysis buffer (5 min, on ice). To isolate the RNA, the lysates were further processed using the Qiagen
423 RNeasy kit with an additional DNAse treatment (30 min, Qiagen, 74106). RNA was eluted in 30 μl RNAse-free H_2O
424 and quantified with a spectrophotometer (NanoDrop, ND-1000, Isogen Life Science, The Netherlands). Total RNA
425 was reverse-transcribed into cDNA in a thermal cycler (protocol: 65 °C (5 min), on ice (2 min) while adding the
426 enzyme mixture, 37 °C (2 min), 25 °C (1 min), 37 °C (50 min), and 70 °C (15 min)). The reaction solution consisted
427 of 200 ng RNA, 1 μL dNTPs (10 mM, Invitrogen), 1 μl random primers (50 ng·μl^{-1}, Promega, C1181), 2 μL 0.1M
428 DTT, 4 μl 5× first strand buffer, and 1 μl M-MLV Reverse Transcriptase (200 U·μl^{-1}, Invitrogen, 28025-013), which
429 was supplemented to 20 μl with RNAse-free H_2O. qPCR was performed in a 10 μl reaction mix, containing 3 μl $100\times$
430 diluted cDNA, 500 nM primer (forward and reversed, see Table SII), and 5 μl SYBR Green Supermix (Bio-Rad,
431 170-8886). Gene expression was normalized to GAPDH, identified as being most stable. C_t values were acquired
432 by exposing the reaction mixtures to the following thermal protocol: 95 °C (3 min), 40 cycles of 95 °C (20 s), 60 °C
433 (20 s), and 72 °C (30 s), 95 °C (1 min), and 65 °C (1 min), concluded with a melting curve measurement. C_t values
434 were normalized for the housekeeping gene (ΔC_t) and control ($\Delta\Delta C_t$, LSS condition), and the $2^{-\Delta\Delta C_t}$ formula
435 was applied to calculate relative fold gene expressions of the genes listed in Table SI.

436 **ELISA.** Intimal hyperplasia-related proteins (Table SI) were quantified from the supernatants at day 14 using a
437 Luminex-based multiplex immunoassay (Multiplex core facility of the laboratory for Translational Immunology,
438 UMC Utrecht, the Netherlands). In short, the supernatants were consecutively incubated with antibody-conjugated
439 MagPlex microspheres (1 h), biotinylated antibodies (1 h), and streptavidin-phycoerythrin (10 min, diluted in high
440 performance ELISA (HPE) buffer (Sanquin)). Fluorescence intensity was measured using a FLEXMAP 3D system
441 and analyzed by five-parametric curve fitting using Bio-Plex Manager software (Biorad, version 6.1.1). Protein
442 concentrations were normalized to the average DNA content per condition.

443 **Statistics.** All data are presented either as mean $\pm$ standard deviation or as boxplots. Statistical analysis was
444 performed to test for significant differences between the different shear stress modes with respect to biochemical
445 content, gene expression, and cytokine secretion using a two-sided non-parametric Kruskal-Wallis test with a Dunn's
446 multiple comparison test (GraphPad, La Jolla, CA, USA). Gene expression data was logarithmically transformed
447 prior to statistical analysis. Statistical significance was assumed for $p < 0.05$.

References

448
449 [1] Quicken S, de Bruin Y, Mees B, Tordoir J, Delhaas T, and Hubert W. Computational study on the haemo-
450   dynamic and mechanical benefits of electrospun polyurethane dialysis grafts. *Biomech Model Mechanobiol*,
451   (19):713–722, 2020.
452 [2] Shiu YT, Rotmans JI, Geelhoed WJ, Pike DB, and Lee T. Arteriovenous conduits for hemodialysis: how to
453   better modulate the pathophysiological vascular response to optimize vascular access durability. *Am J Physiol
454   Renal Physiol*, 316(5):F794–F806, 2019.

[3] Lee T and Roy-Chaudhury P. Advances and new frontiers in the pathophysiology of venous neointimal hyperplasia and dialysis access stenosis. *Adv Chronic Kidney Dis*, 16(5):329–338, 2009.

[4] Haruguchi H and Teraoka S. Intimal hyperplasia and hemodynamic factors in arterial bypass and arteriovenous grafts: a review. *J Artif Organs*, 6(4):227–235, 2003.

[5] Carroll GT, McGloughlin TM, O'Keefe LM, Callanan A, and Walsh MT. Realistic temporal variations of shear stress modulate mmp-2 and mcp-1 expression in arteriovenous vascular access. *Cell Mol Bioeng*, 2(4):591–605, 2009.

[6] Carroll GT, McGloughlin TM, Burke PE, Egan M, Wallis F, and Walsh MT. Wall shear stresses remain elevated in mature arteriovenous fistulas: a case study. *J Biomech Eng*, 133(2):1–9, 2011.

[7] Krishnamoorthy MK, Banerjee RK, Wang Y, Zhang J, Sinha Roy A, Khoury SF, Arend LJ, Rudich S, and Roy-Chaudhury P. Hemodynamic wall shear stress profiles influence the magnitude and pattern of stenosis in a pig av fistula. *Kidney Int*, 74(11):1410–1419, 2008.

[8] Ene-Iordache B and Remuzzi A. Disturbed flow in radial-cephalic arteriovenous fistulae for haemodialysis: low and oscillating shear stress locates the sites of stenosis. *Nephrol Dial Transplant*, 27(1):358–368, 2012.

[9] Rajabi-Jagahrgh E, Krishnamoorthy MK, Wang Y, Choe A, Roy-Chaudhury P, and Banerjee RK. Influence of temporal variation in wall shear stress on intima-media thickening in arteriovenous fistulae. *Semin Dial*, 26(4):511–519, 2013.

[10] Rajabi-Jagahrgh E, Roy-Chaudhury P, Wang Y, Al-Rjoub M, Campos-Naciff B, Choe A, Dumoulin C, and Banerjee RK. New techniques for determining the longitudinal effects of local hemodynamics on the intima-media thickness in arteriovenous fistulae in an animal model. *Semin Dial*, 27(4):424–435, 2014.

[11] Browne LD, Bashar K, Griffin P, Kavanagh EG, Walsh SR, and Walsh MT. The role of shear stress in arteriovenous fistula maturation and failure: a systematic review. *PLoS One*, 10(12):1–24, 2015.

[12] Peiffer V, Sherwin SJ, and Weinberg PD. Does low and oscillatory wall shear stress correlate spatially with early atherosclerosis? A systematic review. *Cardiovasc Res*, 99(2):242–250, 2013.

[13] Kirkton RD, Santiago-Maysonet M, Lawson JH, Tente WE, Dahl SLM, Niklason LE, and Prichard HL. Bioengineered human acellular vessels recellularize and evolve into living blood vessels after human implantation. *Sci Transl Med*, 11:eaau6934, 2019.

[14] van Haaften EE, Bouten CVC, and Kurniawan NA. Vascular mechanobiology: towards control of *in situ* regeneration. *Cells*, 6(3):19, 2017.

[15] van Haaften EE, Wissing TB, Kurniawan NA, Smits AIPM, and Bouten CVC. Human *in vitro* model mimicking material-driven vascular regeneration reveals how cyclic stretch and shear stress differentially modulate inflammation and matrix deposition. *Adv Biosyst*, 4(6):1900249, 2020.

[16] Montini-Ballarin F, Abraham GA, and Caracciolo PC. *Mechanical behavior of polyurethane-based small-diameter vascular grafts*, pages 451–477. Woodhead Publishing, 2016.

[17] Quicken S, Hubert W, Tordoir J, van Loon M, DelHaas T, and Mees B. Computational modelling based recommendation on optimal dialysis needle positioning and dialysis flow in patients with arteriovenous grafts. *Eur J Vasc Endovasc Surg*, 59(2):288–294, 2020.

[18] McGah Patrick M, Leotta Daniel F, Beach Kirk W, and Aliseda Alberto. Effects of wall distensibility in hemodynamic simulations of an arteriovenous fistula. *Biomechanics and modeling in mechanobiology*, 13(3):679–695, 2014.

[19] Decorato Iolanda, Kharboutly Zaher, Vassallo Tommaso, Penrose Justin, Legallais Cécile, and Salsac Anne-Virginie. Numerical simulation of the fluid structure interactions in a compliant patient-specific arteriovenous fistula. *International journal for numerical methods in biomedical engineering*, 30(2):143–159, 2014.

[20] Malek AM, Alper SL, and Izumo S. Hemodynamic shear stress and its role in atherosclerosis. *JAMA*, 282(21):2035–2042, 1999.

[21] van Haaften EE, Wissing TB, Rutten MCM, Bulsink JA, Gashi K, van Kelle MAJ, Smits AIPM, Bouten CVC, and Kurniawan NA. Decoupling the effect of shear stress and stretch on tissue growth & remodeling in a vascular graft. *Tissue Eng Part C*, 24(7), 2018.

[22] Koch SE, van Haaften EE, Wissing TB, Cuypers LAB, Bulsink JA, Bouten CVC, Kurniawan NA, and Smits AIPM. A multi-cue bioreactor to evaluate the inflammatory and regenerative capacity of biomaterials uder flow and stretch. *J Vis Exp*, under review, 2020.

[23] Wisse E, Spiering AJH, van Leeuwen ENM, Renken RAE, Dankers PYW, van Luyn MJA, Harmsen MC, Sommerdijk NAJM, and Meijer EW. Molecular recognition in poly(ε-caprolactone)-based thermoplastic elastomers. *Biomacromolecules*, 7(12):3385–3395, 2006.

[24] van den Broek CN, Pullens RAA, Frøbert O, Rutten MCM, den Hartog WF, and van de Vosse FN. Medium with blood-analog mechanical properties for cardiovascular tissue culturing. *Biorheology*, 45(6):651–661, 2008.

[25] Hata R and Senoo H. L-ascorbic acid 2-phosphate stimulates collagen accumulation, cell proliferation, and formation of a three-dimensional tissuelike substance by skin fibroblasts. *J Cell Physiol*, 138(1):8–16, 1989.

[26] Cheng C, Tempel D, van Haperen R, van der Baan A, Grosveld F, Daemen MJAP, Krams R, and de Crom R. Atherosclerotic lesion size and vulnerability are determined by patterns of fluid shear stress. *Circulation*, 113(23):2744–2753, 2006.

[27] Cheng C, Tempel D, van Haperen R, de Boer HC, Segers D, Huisman M, van Zonneveld AJ, Leenen PJM, van der Steen AFW, Serruys PW, de Crom R, and Krams R. Shear stress-induced changes in atherosclerotic plaque composition are modulated by chemokines. *J Clin Invest*, 117(3):616–626, 2007.

[28] Seneviratne AN, Cole JE, Goddard ME, Park I, Mohri Z, Sansom S, Udalova I, Krams R, and Monaco C. Low shear stress induces M1 macrophage polarization in murine thin-cap atherosclerotic plaques. *J Mol Cell Cardiol*, 89:168–172, 2015.

[29] Cheng C, Helderman F, Tempel D, Segers D, Hierck BP, Poelmann RE, van Tol A, Duncker DJ, Robbers-Visser D, Ursem NTC, van Haperen R, Wentzel JJ, Gijsen F, van der Steen AFW, de Crom R, and Krams R. Large variations in absolute wall shear stress levels within one species and between species. *Atherosclerosis*, 195(2):225–235, 2007.

[30] Vogel C and Marcotte EM. Insights into the regulation of protein abundance from proteomic and transcriptomic analyses. *Nature Rev Genet*, 13(4):227–232, 2012.

[31] Wissing TB, Bonito V, van Haaften EE, van Doeselaar M, Brugmans MCP, Janssen HM, Bouten CVC, and Smits AIPM. Macrophage-driven biomaterial degradation depends on scaffold microarchitecture. *Front Bioeng Biotechnol*, 7:87, 2019.

[32] Wissing TB, Haaften EE van, Koch SE, Ippel B, Kurniawan NA, Bouten CVC, and Smits AIPM. Hemodynamic loads distinctively impact the secretory profile of biomaterial-activated macrophages –implications for in situ vascular tissue engineering. *Biomater Sci*, 8(1):132–147, 2019.

[33] Butler HJ, Ashton L, Bird B, Cinque G, Curtis K, Dorney J, Esmonde-White K, Fullwood NJ, Gardner B, Martin-Hirsch PL, Walsh MJ, McAinsh MR, Stone N, and Martin FL. Using Raman spectroscopy to characterize biological materials. *Nat Protoc*, 11(4):664–687, 2016.

[34] Ramachandra AB, Humphrey JD, and Marsden AL. Gradual loading ameliorates maladaptation in computational simulations of vein graft growth and remodelling. *J R Soc Interface*, 14(130):20160995, 2017.

[35] Ramachandra AB, Sankaran S, Humphrey JD, and Marsden AL. Computational simulation of the adaptive capacity of vein grafts in response to increased pressure. *J Biomech Eng*, 137(3):31009, 2015.

[36] Mortensen M and Valen-Sendstad K. Oasis: A high-level/high-performance open source Navier-Stokes solver. *Comput Phys Commun*, 188:177–188, 2015.

[37] Logg A, Mardal K, and Wells GN. *Automated Solution of Differential Equations by the Finite Element Method*, volume 84. Springer-Verlag Berlin Heidelberg, 2012.

[38] Hoffman J, Jansson J, Abreu RV de, Degirmenci NC, Jansson N, Müller K, Nazarov M, and Spühler JH. Unicorn: Parallel adaptive finite element simulation of turbulent flow and fluid-structure interaction for deforming domains and complex geometry. *Comput Fluid*, 80:310–319, 2013.

[39] Schnell AM, Hoerstrup SP, Zünd G, Kolb S, Sodian R, Visjager JF, Grunenfelder J, Suter A, and Turina MI. Optimal cell source for cardiovascular tissue engineering: venous vs. aortic human myofibroblasts. *Thorac Cardiovasc Surg*, 49(4):221–225, 2001.

[40] Mol A, Rutten MCM, Driessen NJB, Bouten CVC, Zünd G, Baaijens FPT, and Hoerstrup SP. Autologous human tissue-engineered heart valves: prospects for systemic application. *Circulation*, 114(suppl I):152–158, 2006.

[41] Mol A, van Lieshout MI, Dam-de Veen CG, Neuenschwander S, Hoerstrup SP, Baaijens FPT, and Bouten CVC. Fibrin as a cell carrier in cardiovascular tissue engineering applications. *Biomaterials*, 26(16):3113–3121, 2005.

[42] Farndale RW, Buttle DJ, and Barrett AJ. Improved quantitation and discrimination of sulphated glycosaminoglycans by use of dimethylmethylene blue. *Biochim Biophys Acta*, 883(2):173–177, 1986.

[43] Huszar G, Maiocco J, and Naftolin F. Monitoring of collagen and collagen fragments in chromatography of protein mixtures. *Anal Biochem*, 105(1):424–429, 1980.

[44] Boerboom RA, Krahn KN, Megens RTA, van Zandvoort MAMJ, Merkx M, and Bouten CVC. High resolution imaging of collagen organisation and synthesis using a versatile collagen specific probe. *J Struct Biol*, 159(3):392–399, 2007.

AUTHOR CONTRIBUTIONS

CB and NK contributed equally. Author contributions according to the CRediT Taxonomy are as follows: Conceptualization: All; Formal Analysis: EH, CB, NK; Investigation: EH, SQ; Funding Acquisition: CB; Supervision: NK, CB; Visualization: EH; Writing – Original Draft Preparation: EH; Writing – Review & Editing: All. All authors have approved the final article.

ADDITIONAL INFORMATION

Competing financial interests: The authors declare no competing financial interests.

Data availability statement: The data that support the findings of this study are available from the corresponding author upon reasonable request.

Code availability statement: The code to obtain and analyze the data that support the findings of this study are available from the corresponding author upon reasonable request.
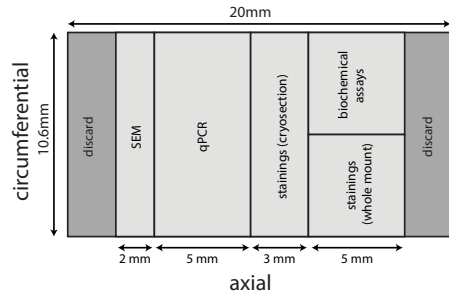
SUPPLEMENTARY INFORMATION
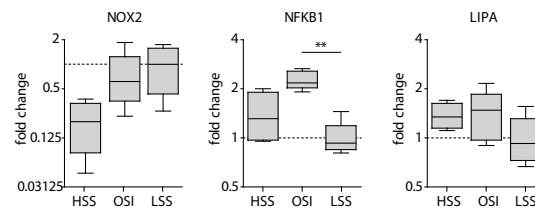

FIGURE SI. **Cutting scheme for day 14 scaffolds.**

FIGURE SII. **Gene expression analysis of degradation after 14 days of dynamic culture.** HSS, high shear stress condition (3.2 Pa); OSS, oscillatory shear stress condition ($\pm$3.2 Pa); LSS, low shear stress condition (0.4 Pa) ($n = $ 4–5/group, * $p < 0.05$, ** $p < 0.01$).
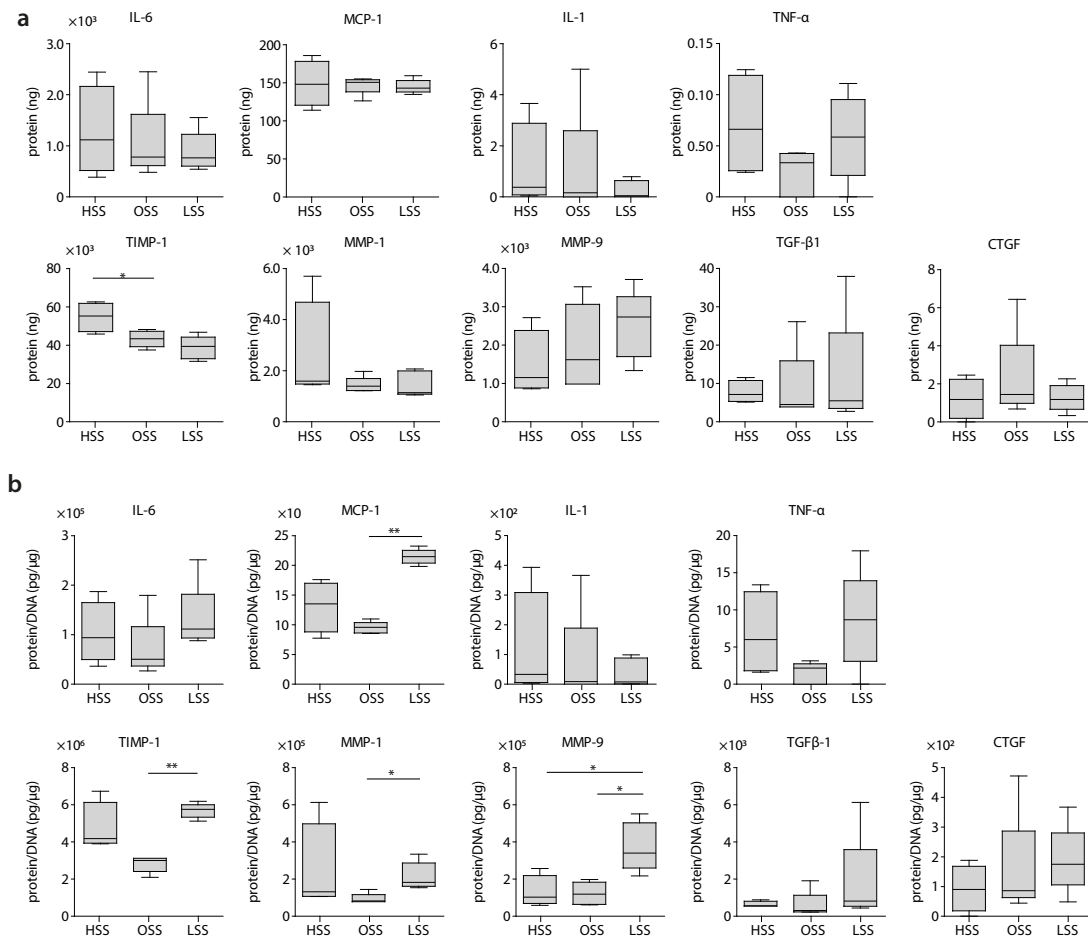
FIGURE SIII. **Secretion profiles of intimal hyperplasia- and tissue formation-related proteins at day 14.** **(a)** Total protein production in the culture medium and **(b)** protein production in the culture medium normalized to DNA content. HSS, high shear stress condition (3.2 Pa, $n = 4$); OSS, oscillatory shear stress condition ($\pm$3.2 Pa, $n = 5$); LSS, low shear stress condition (0.4 Pa, $n = 5$) (* $p < 0.05$, ** $p < 0.01$).
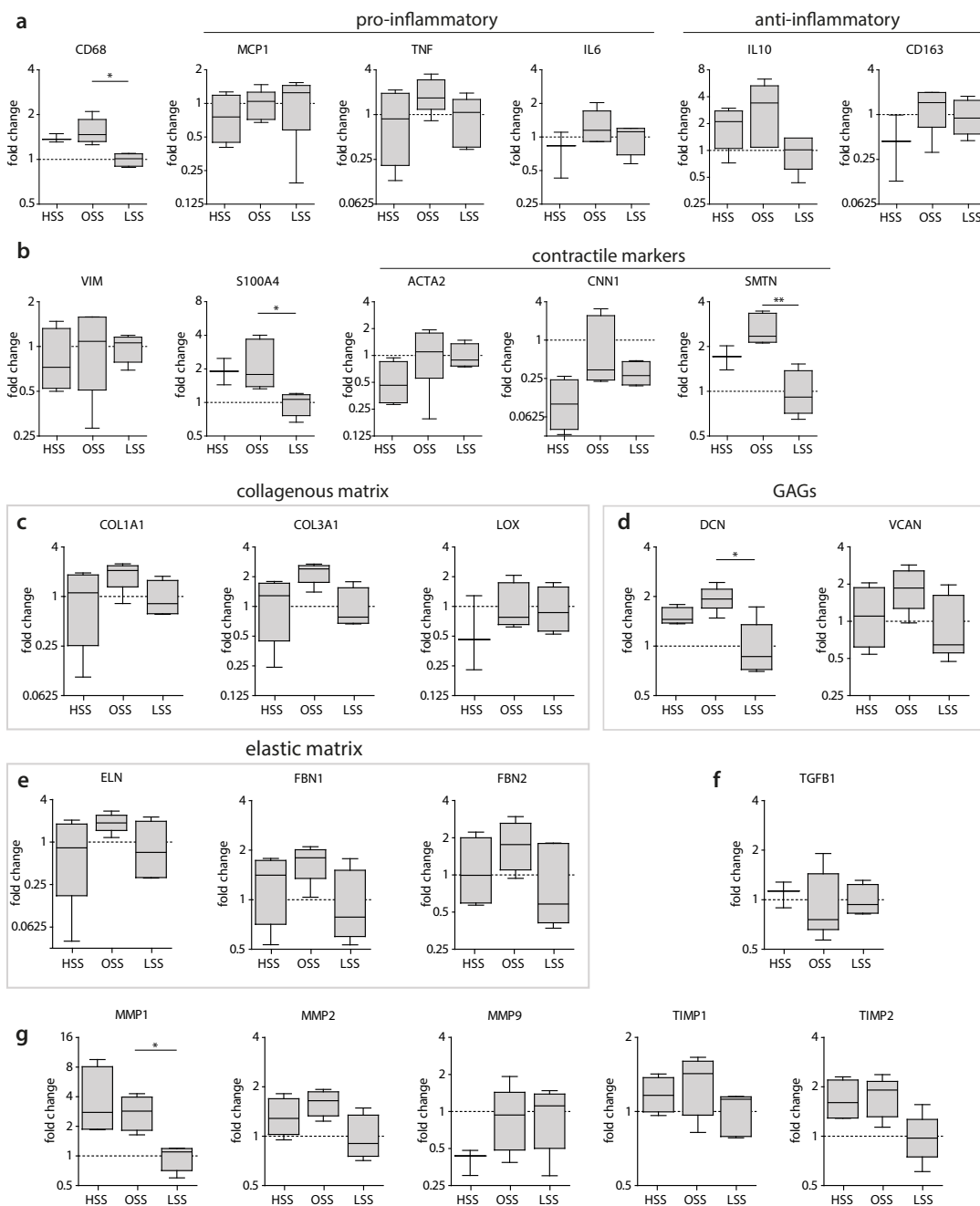
FIGURE SIV. **Gene expression analysis of phenotypical, growth, and remodeling markers after 14 days of dynamic culture.** Relative gene expression compared to the low shear stress condition for **(a)** macrophage-related genes, **(b)** (myo)fibroblast-related genes, **(c)** collageneous matrix- related genes, **(d)** GAGs-related genes, **(e)** elastic matrix-related genes, **(f)** TGFB1, and **(g)** proteases ($n = 3$–5/group, * $p < 0.05$, ** $p < 0.01$).

Protein	Symbol	Function	qPCR	ELISA
Phenotypic markers				
Cluster of differentiation 68	CD68	Pan-macrophage marker	×	
Cluster of differentiation 163	CD163	Anti-inflammatory macrophage marker	×	
Monocyte chemoattractant protein 1	MCP-1	Chemotactic for monocytes/macrophages	×	×
Tumor necrosis factor α	TNF-α	Pro-inflammatory factor, stimulus for collagen production, inhibitor of elastogenesis	×	×
Interleukin 1	IL-1	Neutrophil/monocyte recruitment		×
Interleukin 6	IL-6	Pro-inflammatory factor	×	×
Interleukin 10	IL-10	Anti-inflammatory cytokine, inhibitor of collagen production	×	
α smooth muscle actin	αSMA	Filament of the cytoskeleton involved in regulating cell shape, movement and involved in cell contractility	×	
Smoothelin	SMTN	Constitutes part of the cytoskeleton and is found exclusively in contractile smooth muscle cells	×	
Calponin	CNN1	Protein that is involved in the modulation and regulation of smooth muscle cell contraction	×	
S100 calcium binding protein A4	S100A4	Protein involved in the regulation of multiple cellular processes (e.g., cell cycle progression, differentiation, tubulin polymerization). Activated fibroblast, regulated to tissue remodeling	×	
Vimentin	VIM	Intermediate filament protein, part of the cytoskeleton, used as fibroblast marker	×	
Tissue formation				
Transforming growth factor β	TGF-β1	Anti-inflammatory factor; stimulus for collagen formation	×	×
Connective tissue growth factor	CTGF	Stimulus for collagen formation		×
Collagen type I	COL1A1	Load bearing protein of the extracellular matrix	×	
Collagen type III	COL3A1	A fibrillary collagen; found frequently in association with type I collagen	×	
Lysyl oxidase	LOX	Enzyme involved in collagen and elastin crosslinking	×	
Elastin	ELN	Tropoelastin, one of the main components of the elastic fiber	×	
Fibrillin 1	FBN-1	Extracellular matrix protein that provides structural support for elastic fibril formation	×	
Fibrillin 2	FBN-2	Extracellular matrix protein that provides structural support for elastic fibril formation	×	
Decorin	DCN	Proteoglycan important in collagen fibril assembly	×	
Versican	VCAN	Proteoglycan important for cell adhesion, proliferation, differentiation and migration. Proven important for elastic network formation	×	
Remodeling				
Matrix metalloproteinase 1	MMP-1	Extra-cellular breakdown and remodeling	×	×
Matrix metalloproteinase 2	MMP-2	Extra-cellular breakdown and remodeling	×	
Matrix metalloproteinase 9	MMP-9	Anti-inflammatory factor involved in extra-cellular breakdown and remodeling	×	×
Metallopeptidase inhibitor 1	TIMP-1	Inhibitor of MMPs	×	×
Metallopeptidase inhibitor 2	TIMP-2	Inhibitor of MMPs	×	
Degradation				
Nicotinamide adenine dinucleotide phosphate-oxidase 2	NOX2	Enzyme complex that contributes to ROS production	×	
Nuclear factor κ-light-chain-enhancers of activated B cells	NFκβ	Involved in cellular responses to oxidative stress and cell survival	×	
Lipase A or cholesterol ester hydrolase	LIPA	Lysosomal enzyme	×	

TABLE SI. Genes and proteins analyzed via qPCR (primer sequences in Table SII) and Multiplex ELISA

Primer	Symbol	Accession number	Primer sequence ('5-'3)
Phenotypic markers			
Cluster of differentiation 68	CD68	NM_001040059.1	FW: CTACTGGCAGAGAGCACTGG RV: CCGCCATGTAGCTCAGGTAG
Cluster of differentiation 163	CD163	NM_004244	FW:CACTATGAAGAAGCCAAAATTACCT RV: AGAGAGAAGTCCGAATCACAGA
Monocyte chemoattractant protein 1	MCP-1	NM_002982	FW: CAGCCAGATGCAATCAATGCC RV: TGGAATCCTGAACCCACTTCT
Tumor necrosis factor α	TNF	NM_000594	FW: GAGGCCAAGCCCTGGTATG RV: CGGGCCGATTGATCTCAGC
Interleukin 6	IL6	NM_000600	FW: ACTCACCTCTTCAGAACGAATTG RV: GTCGAGGATGTACCGAATTTGT
Interleukin 10	IL10	NM_000572	FW: GACTTTAAGGGTTACCTGGGTTG RV: TCACATGCGCCTTGATGTCTG
α smooth muscle actin	ACTA2	NM_001613.1	FW: CGTGTTGCCCCTGAAGAGCAT RV: ACCGCCTGGATAGCCACATACA
Smoothelin	SMTN	NM_134270	FW: CAGCCCAGAACCGAGAGTC RV: AGCAGCCATAGGAGAATCAGAT
Calponin	CNN1	NM_001299.5	FW:TGAAGTACGCAGAGAAGCAG RV:CAGCTTGGGGTCGTAGAG
S100 calcium binding protein A4	S100A4	NM_002961	FW:TCTTTCTTGGTTTGATCCTGACT RV: AGTTCTGACTTGTTGAGCTTGA
Vimentin	VIM	NM_003380	FW: AAGACCTGCTCAATGTTAAGATC RV: CTGCTCTCCTCGCCTTCC
Tissue formation			
Transforming growth factor β	TGFB1	NM_000660	FW: GCAACAATTCCTGGCGATACCTC RV: AGTTCTTCTCCGTGGAGCTGAAG
Collagen type I	COL1A1	NM_000088	FW: AATCACCTGCGTACAGAACGG RV: TCGTCACAGATCACGTCATCG
Collagen type III	COL3A1	NM_000090	FW: ATCTTGGTCAGTCCTATGC RV: TGGAATTTCTGGGTTGGG
Lysyl oxidase	LOX	NM_002317.3	FW:CCTGGCTGTTATGATAC RV: GAGGCATACGCATGATG
Elastin	ELN	NM_000501.3	FW: CTGGAATTGGAGGCATCG RV: TCCTGGGACACCAACTAC
Fibrillin 1	FBN1	NM_00138	FW:TGTTGGTTTGTGAAGATATTG RV: GTGGAGGTGAAGCGGTAG
Fibrillin 2	FBN2	NM_001999	FW:ATCCCTGTGAGATGTGTC RV: TTCCTCCTTGGCATATCC
Decorin	DCN	NM_133503	FW:TGCAGCTAGCCTGAAAGGAC RV: TTGGCCAGAGAGCCATTGTC
Versican	VCAN	NM_004385	FW:GGCACCTGTTATCCTACTGAAA RV: ACACAAGTGGCTCCATTACG
Tissue remodeling			
Matrix metalloproteinase 1	MMP1	NM_001145938.1	FW:CGCACAAATCCCTTCTACCC RV: CTGTCGGCAAATTCGTAAGC
Matrix metalloproteinase 2	MMP2	NM_001127891	FW: ATGACAGCTGCACCACTGAG RV: ATTTGTTGCCCAGGAAAGTG
Matrix metalloproteinase 9	MMP9	NM_004994	FW: TGGGGGGCAACTCGGC RV: GGAATGATCTAAGCCCAG
Metallopeptidase inhibitor 1	TIMP1	NM_003254.2	FW: TGACATCCGGTTCGTCTACA RV: TGCAGTTTTCCAGCAATGAG
Metallopeptidase inhibitor 2	TIMP2	NM_003255.4	FW:GGAGGAATCGGTGAGGTC RV: AACAGGCAAGAACAATGG
Construct degradation			
Nicotinamide adenine dinucleotide phosphate-oxidase 2	NOX2	NM_000397.3	FW:AACTGGGCTGTGAATGAGGG RV: GCCAGTGCTGACCCAAGAA
Nuclear factor κ-light-chain-enhancers of activated B cells	NFKB1	NM_001165412	FW:AGACCAAGGAGATGGACCTCA RV: GCATTGGGGGCTTTACTGTC
Lipase A or cholesterol ester hydrolase	LIPA	NM_001288979.1	FW:TCCTGCTGGAACTTCTGTGC RV: ACTGCTTCCCCAGTCAAAGG

TABLE SII. Primers used for gene expression analysis